

Rapid Particle Acceleration due to Recollimation Shocks and Turbulent Magnetic Fields in Injected Jets with Helical Magnetic Fields

Kenichi Nishikawa,¹[★] Yosuke Mizuno,² Jose L. Gómez,³ Ioana Duţan,⁴
Jacek Niemiec,⁵ Oleh Kobzar,⁵ Nicholas MacDonald,⁶ Athina Meli,^{7,8}
Martin Pohl⁹ and Kouichi Hirotani¹⁰

¹*Department of Physics, Chemistry and Mathematics, Alabama A&M University, Normal, AL 35762, USA*

²*Institute for Theoretical Physics, Goethe University, D-60438 Frankfurt am Main, Germany*

³*Instituto de Astrofísica de Andalucía, CSIC, Apartado 3004, 18080 Granada, Spain*

⁴*Institute of Space Science, Atomîştilor 409, RO-077125 Bucharest-Măgurele, Romania*

⁵*Institute of Nuclear Physics Polish Academy of Sciences, PL-31342 Krakow, Poland*

⁶*Max-Planck-Institut für Radioastronomie, Auf dem Hügel 69, D-53121 Bonn, Germany*

⁷*Space Sciences & Technologies for Astrophysics Research (STAR) Institute Université de Liège, Sart Tilman, 4000 Liège, Belgium*

⁸*Department of Physics and Astronomy, University of Gent, 9000 Gent, Belgium*

⁹*Institute of Physics and Astronomy, University of Potsdam, 14476 Potsdam-Golm, and DESY, Platanenallee 6, 15738 Zeuthen, Germany*

¹⁰*Academia Sinica, Institute of Astronomy and Astrophysics (ASIAA), PO Box 23-141, Taipei, Taiwan*

Accepted 2020 February 5. Received 2020 January 17; in original form 2019 October 15

ABSTRACT

One of the key questions in the study of relativistic jets is how magnetic reconnection occurs and whether it can effectively accelerate electrons in the jet. We performed 3D particle-in-cell (PIC) simulations of a relativistic electron-proton jet of relatively large radius that carries a helical magnetic field. We focussed our investigation on the interaction between the jet and the ambient plasma and explore how the helical magnetic field affects the excitation of kinetic instabilities such as the Weibel instability (WI), the kinetic Kelvin-Helmholtz instability (kKHI), and the mushroom instability (MI). In our simulations these kinetic instabilities are indeed excited, and particles are accelerated. At the linear stage we observe recollimation shocks near the center of the jet. As the electron-proton jet evolves into the deep nonlinear stage, the helical magnetic field becomes untangled due to reconnection-like phenomena, and electrons are repeatedly accelerated as they encounter magnetic-reconnection events in the turbulent magnetic field.

Key words: numerical – jets and outflows – relativistic processes – magnetic reconnection – turbulence – acceleration of particles

1 INTRODUCTION

Magnetic reconnection is ubiquitous in solar and magnetospheric plasmas, and it has been proposed that it is also an important mechanism for particle acceleration in Active Galactic Nuclei (AGN) and gamma-ray burst jets (Drenkhahn & Spruit 2002; de Gouveia Dal Pino & Lazarian 2005; de Gouveia Dal Pino et al. 2010; Uzdensky 2011; Granot et al. 2011; Granot 2012; McKinney & Uzdensky 2012; Zhang & Yan 2011; Giannios et al. 2009; Giannios

2010, 2011; Komissarov 2012; Sironi et al. 2015; de Gouveia Dal Pino et al. 2018; Kadowaki et al. 2018, 2019; Christie et al. 2019; Fowler et al. 2019). To study the fundamental physics of magnetic reconnection, numerous particle-in-cell (PIC) simulations have been performed that use the Harris model in a slab geometry (e.g., Daughton 2011; Wendel et al. 2013; Karimabadi et al. 2014; Zenitani & Hoshino 2005, 2008; Zenitani et al. 2011, 2013; Oka et al. 2008; Fujimoto 2011; Kagan et al. 2013; Sironi & Spitkovsky 2011, 2014; Guo et al. 2015, 2016a,b). Generally, studies in the slab configuration show significant particle acceleration. However, this configuration does not apply to astrophysical jets, since the magnetic field appears to have a helical morphology close

[★] E-mail: kenichi.nishikawa@aamu.edu(KN)

to the jet collimation/launching point (e.g., Tchekhovskoy 2015; Hawley et al. 2015; Gabuzda 2019).

In jets MHD instabilities such as Kelvin-Helmholtz (KHI) and the kink instability (KI) can operate (e.g., Birkinshaw 1984, 1996; Stone & Norman 1994; Stone & Hardee 2000). Recently, these MHD instabilities have been revisited using PIC simulations including kinetic processes (e.g., Sironi et al. 2013; Alves et al. 2015; Ardaneh et al. 2016; Nishikawa et al. 2019).

The interaction of relativistic jets with the plasma environment generates relativistic shocks that are mediated by the Weibel instability (WI) and accelerate particles. At the velocity-shear boundary between the jet and the ambient medium magnetic turbulence is generated by the kinetic Kelvin-Helmholtz (kKHI) and the mushroom (MI) instability. Recent PIC simulations explored the WI, kKHI and MI in slab models of jets and later focussed on the evolution of cylindrical jets in helical magnetic-field geometry (e.g., Sironi et al. 2013; Alves et al. 2015; Ardaneh et al. 2016; Nishikawa et al. 2019). To achieve a complete understanding of the physics within the jet, global three-dimensional (3D) modeling needs to be performed that enables investigation of the combined shock/shear layer processes and includes kinetic effects. Our first PIC simulations of global jets were performed for unmagnetized plasmas (Nishikawa et al. 2016a). With this work we extend these studies to jets containing helical magnetic field.

One of the key questions we want to answer is how the helical magnetic field affects the growth of the kKHI, MI, and WI, and how and where in the jet structure particles are accelerated. In the latter respect, we are particularly interested in magnetic reconnection and its ability to aid in the rapid merging and breaking of the helical magnetic field carried by relativistic jets. Relativistic magneto-hydrodynamic (RMHD) simulations demonstrate that jets with helical field develop kink instabilities (KI) (e.g., Mizuno et al. 2014; Singh et al. 2016; Barniol Duran et al. 2017; de Gouveia Dal Pino et al. 2018; Kadowaki et al. 2018, 2019); similar structures were found in PIC simulations (see, e.g., Nishikawa et al. 2019). It should be noted that MHD instabilities such as KHI and KI in jets have been investigated extensively (e.g., Birkinshaw 1984; Stone & Norman 1994; Stone & Hardee 2000; Hawley et al. 2015). PIC simulations of a single flux rope modeling the jet that undergoes internal KI showed signatures of secondary magnetic reconnection (Markidis et al. 2014).

Recently, it was demonstrated that the development of the KI in relativistic strongly magnetized jets with helical magnetic field leads to the formation of highly tangled magnetic field and a large-scale inductive electric field promoting the rapid energization of particles through curvature drift acceleration (Alves et al. 2018, 2019). As initial condition these simulations assumed helical magnetic field in the jet frame supported by counter-streaming electrons and positrons (ions). There is neither velocity shear nor a jet head in their simulation, and so no velocity-shear instability such as kKHI and MI can be excited.

In this work we present results of our new study of relativistic jets containing helical magnetic field, which exhibit the nonlinear evolution of kinetic instabilities, magnetic reconnection, and the associated particle acceleration. We focus on electron-scale phenomena and set the jet size suffi-

cient to accommodate the relevant electron kinetic instabilities that are not included in MHD simulations. The kinetic instabilities grow to the nonlinear stage, which is demonstrated by the disappearance of the helical magnetic field. Although our simulation results are insufficient to model the large-scale plasma flows of macroscopic parsec-scale jets, they explore relevant kinetic-scale physics within relativistic jet plasma.

2 PIC SIMULATION SETUP OF A JET WITH HELICAL MAGNETIC FIELD STRUCTURE

In our simulations a cylindrical jet containing helical magnetic field and propagating in the x -direction is injected into an ambient plasma at rest, as is shown schematically in Fig. 6a in Nishikawa et al. (2019). The structure of the helical magnetic field is implemented in the same way as in the RMHD simulations by Mizuno et al. (2014), where a force-free expression of the field at the jet orifice is used. The magnetic field is thus not generated self-consistently by a rotating black hole, as in GRMHD simulations of jet formation. The initial helical magnetic field has the same form as in Equations (1) and (2) of Mizuno et al. (2014),

$$B_x = \frac{B_0}{[1 + (r/a)^2]}, \quad B_\phi = \frac{(r/a)B_0}{[1 + (r/a)^2]}, \quad (1)$$

where r is the radial coordinate in cylindrical geometry, B_0 parametrizes the magnetic-field strength, and a is the characteristic radius of the magnetic field (Nishikawa et al. 2019). Note that for a constant magnetic pitch, $\alpha = 1$, the toroidal field component has a maximum at $r = a$. The toroidal component of the magnetic field in the jet is created by an electric current, $+J_x(y, z)$, in the positive x -direction. In Cartesian coordinates (used in our simulation) the corresponding B_y and B_z field components are defined as:

$$B_y(y, z) = \frac{((z - z_{jc})/a)B_0}{[1 + (r/a)^2]}, \quad B_z(y, z) = -\frac{((y - y_{jc})/a)B_0}{[1 + (r/a)^2]}. \quad (2)$$

Here, the center of the jet is located at (y_{jc}, z_{jc}) , and $r = \sqrt{(y - y_{jc})^2 + (z - z_{jc})^2}$. Equation 2 defines the helicity of the magnetic field that has a left-handed polarity for positive B_0 . At the jet orifice, the helical magnetic field is computed without motional electric fields. This corresponds to magnetic-field generation by jet particles moving in the $+x$ -direction.

The simulated jet has a radius r_{jet} and is assumed to propagate in an initially unmagnetized ambient medium. For the fields external to the jet we use a damping function, $\exp[-(r - r_{\text{jet}})^2/b](r \geq r_{\text{jet}})$, that multiplies the expressions in Equation 2 with the tapering parameter $b = 200\Delta$, where Δ is the grid scale. We further assume a characteristic radius $a = 0.25 * r_{\text{jet}}$. The profiles of the resulting helical magnetic field components are shown in Figure 6b in Nishikawa et al. (2019). The toroidal magnetic field vanishes at the center of the jet (red line in Fig. 6b of Nishikawa et al. (2019)). Note, that the simulation setup adopted in this work has been used in our preliminary studies of helical jets (Nishikawa et al. 2016b, 2017, 2019) with the modifications $B_0 = 0.1$ and $r_{\text{jet}} = 100$.

The jet head assumed here has a flat-density top-hat shape which is a strong simplification of the true structure of the jet-formation region (e.g., Broderick & Loeb 2009;

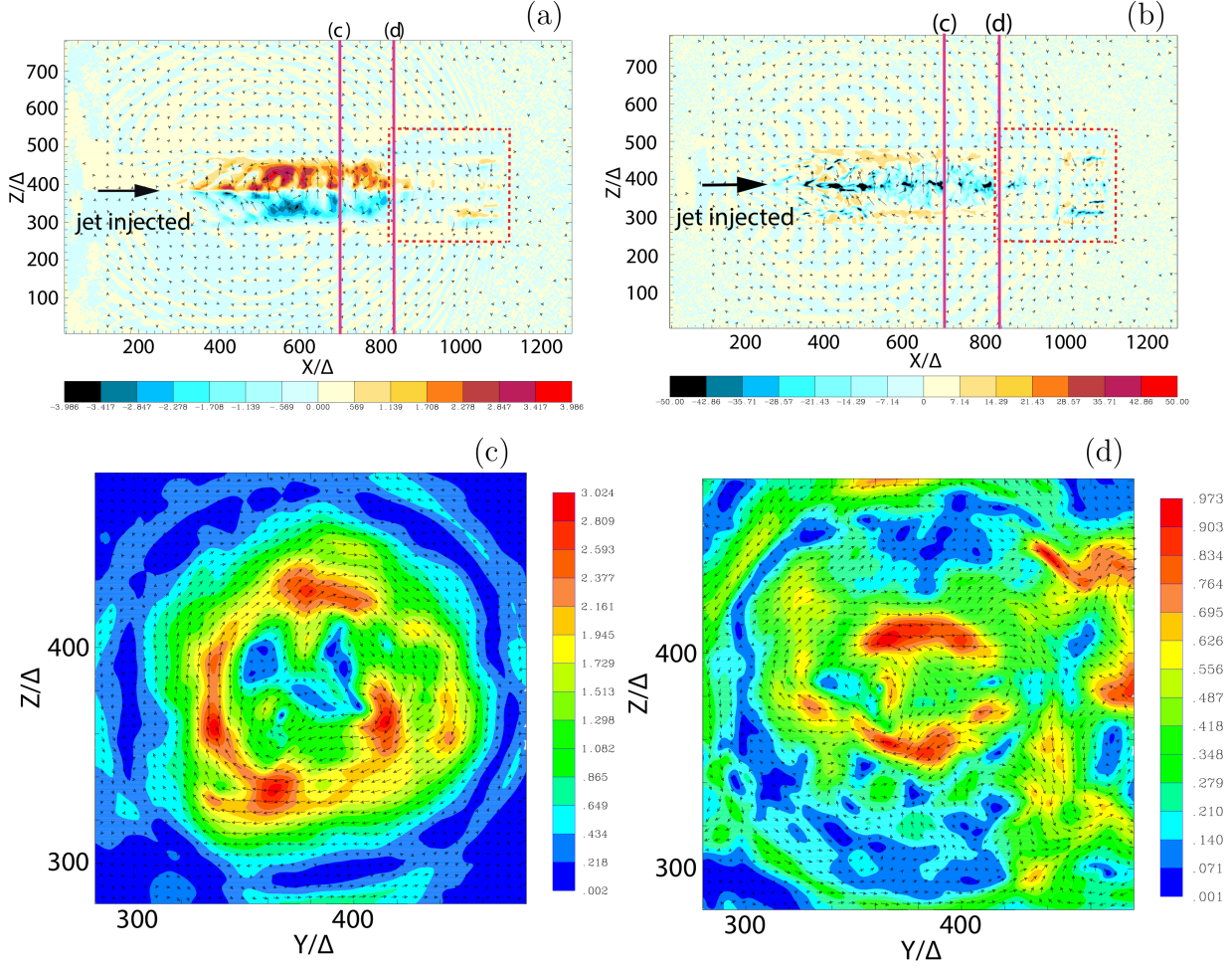


Figure 1. Upper panels: (a) the y -component of the magnetic field, B_y , with x - z electric field depicted by arrows, and (b) the x -component of the electron current density, J_x , with the x - z magnetic field as arrows, both in the $x - z$ plane at $t = 1000 \omega_{pe}^{-1}$. The lower panels show the total magnetic-field strength in the $y - z$ plane at $x/\Delta = 700$ (c) and $x/\Delta = 835$ (d). The arrows indicate the magnetic field (B_y, B_z).

Moscibrodzka et al. 2017). A more realistic jet structure (with, e.g., a Gaussian-shaped head) will be implemented in future studies.

The numerical code we use is a modified version of the relativistic electromagnetic PIC code TRISTAN (Buneman 1993) with MPI-based parallelization (Niemiec et al. 2008). The simulations are performed in Cartesian coordinates on a numerical grid of size $(L_x, L_y, L_z) = (1285\Delta, 789\Delta, 789\Delta)$. We use open boundaries at the $x/\Delta = 0$ and $x/\Delta = 1285$ surfaces and impose periodic boundary conditions in the transverse directions. Since the jet is located at the center of the numerical box far from the boundaries and the simulation is rather short, there are no visible effect of the periodic boundary conditions on the system.

The jet radius is $r_{jet} = 100\Delta$. The jet is injected at $x = 100\Delta$ in the center of the $y - z$ plane. The large computational box allows us to follow the jet evolution long enough to permit the investigation of the strongly nonlinear stage. The longitudinal box size, L_x , and the simulation time, $t_{max} = 1000 \omega_{pe}^{-1}$, are a factor of two larger than in our previous studies (Nishikawa et al. 2016b, 2017, 2019), in which jets with radii $r_{jet} = 20, 40, 80, 120\Delta$ were investigated.

We know that jets of different plasma composition exhibit distinct dynamical behavior that manifests itself in the morphologies of the jet and its emission characteristics (Nishikawa et al. 2016a,b, 2017, 2019). In this report we discuss only electron-proton plasma in both the jet and the ambient medium. The initial particle number per cell is $n_{jt} = 8$ and $n_{am} = 12$, respectively, for the jet and ambient plasma. The electron skin depth is $\lambda_{se} = c/\omega_{pe} = 10.0\Delta$, where c is the speed of light, $\omega_{pe} = (e^2 n_{am}/\epsilon_0 m_e)^{1/2}$ is the electron plasma frequency; the electron Debye length of ambient electrons is $\lambda_D = 0.5\Delta$. The thermal speed of jet electrons is $v_{jt,th,e} = 0.014c$ in the jet reference frame; in the ambient plasma it is $v_{am,th,e} = 0.03c$. We assume temperature equilibration, and so the thermal speed of ions is smaller than that of electrons by the factor $(m_p/m_e)^{1/2}$. We use the realistic proton-to-electron mass ratio $m_p/m_e = 1836$. The jet plasma is initially weakly magnetized, and the magnetic field amplitude parameter assumed, $B_0 = 0.1c$, corresponds to plasma magnetization $\sigma = B^2/n_e m_e \gamma_{jt} c^2 = 2.8 \times 10^{-3}$. The jet Lorentz factor is $\gamma_{jt} = 15$.

3 STRUCTURE OF HELICALLY MAGNETIZED JETS

Figure 1 shows cross-sections through the center of the jet at time $t = 1000 \omega_{pe}^{-1}$ with (a) the y -component of the magnetic field, B_y , with the x - z electric field as arrows, and (b), the x -component of the electron current density, J_x , with the x - z magnetic field depicted as arrows. The jet propagates from the left to right. Very strong helical magnetic field in the jet is evident at $400 \lesssim x/\Delta \lesssim 830$. The amplitude is with $B/B_0 \approx 40$ (Fig. 1a) much larger than that of the initial field. As in the unmagnetized case (Nishikawa et al. 2016a), this field results from MI and kKHI. However, in the presence of the initial helical magnetic field the growth rate of the transverse MI mode is reduced, and the field structure is strongly modulated by longitudinal kKHI wave modes as shown by the bunched B_y field (Fig. 1a). This causes multiple collimations along the jet that are caused by pinching of the jet electrons toward the center of the jet, as visible in the electron current density (Fig. 1b). It should be noted that in Fig 1b the color scale for J_x does not extend beyond $J_x = -50$, as we intend to show the weak positive (return) current. The collimations become weaker further along the jet and eventually disappear at $x/\Delta \gtrsim 830$. At this point B_y is weak. This demonstrates that the nonlinear saturation of the MI leads to the dissipation of the helical magnetic field.

We selected possible reconnection sites in Figures 1a-b, indicated by the two red lines at $x/\Delta = 700$ and $x/\Delta = 835$, and show the magnetic-field structure in the y - z plane in figure panels 1c and 1d, respectively. At $x/\Delta = 700$ clockwise-circular magnetic field is split near the jet into a number of magnetic structures, which demonstrate the growth of MI. They are surrounded by field of opposite polarity that is produced by the proton current framing the jet boundary (see Nishikawa et al. 2016a). The magnetic field at $x = 835\Delta$ is strongly turbulent; its helical structure is distorted and reorganised into multiple magnetic islands, which reflect the nonlinear stage of MI and kKHI. The magnetic islands interact with each other, providing conditions for magnetic reconnection. In our 3D geometry reconnection does not occur at a simple X-point as in 2D slab geometry. Instead, reconnection sites can be identified with regions of weak magnetic field surrounded by oppositely directed magnetic field lines. An example of a possible location of reconnection can be found at $(y/\Delta, z/\Delta) = (380, 340)$, where the total magnetic field becomes minimal (the null point, Fig. 1d). The evolution of the magnetic field at different locations in the jet ($600 < x/\Delta < 1100$) is shown in the supplemental movie. Note that the filamentary structure at the jet head (Fig. 1a-b) is formed by the electron WI. One can see in the movie that nonlinear evolution of the filaments also leads to the appearance of the magnetic structures that are prone to reconnection.

In Figure 2 we show three-dimensional isosurfaces of the x -component of the electron current density at the jet head together with magnetic field lines plotted in yellow. Two rectangles indicate the visible area in the jet. Near the jet head, the current filaments generated by the WI are evident. This result is similar to that obtained by Ardaneh et al. (2016) (their Fig. 3), who investigate the structure of the head of an electron-ion jet in slab geometry with $m_i/m_e = 16$. They demonstrated the acceleration of jet electrons in the

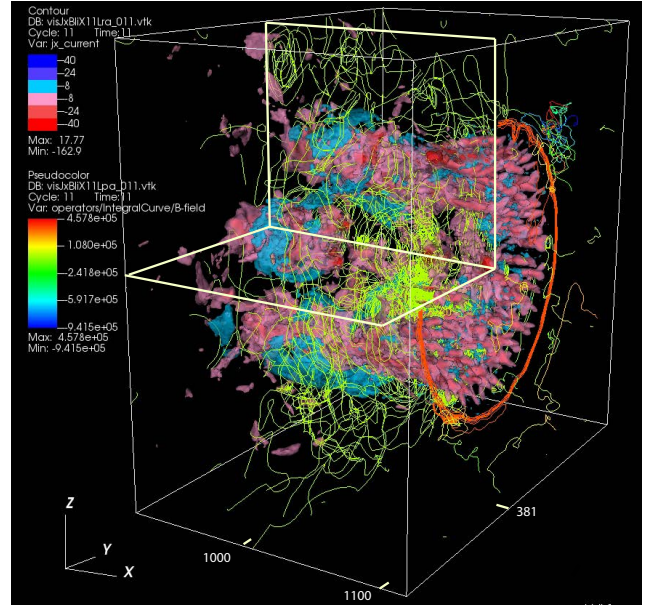


Figure 2. Isosurface of the x -component of the electron current density, J_x , with the magnetic field lines (yellow) in a rectangular section of the simulation grid ($920 < x/\Delta < 1120$; $231 < y/\Delta, z/\Delta < 531$) at time $t = 1000 \omega_{pe}^{-1}$. To illustrate the distribution of J_x inside the jet, a quadrant of the regions is clipped at the center of the jet in the x - z plane ($381 < z/\Delta < 531$) and in the x - y plane ($231 < y/\Delta < 381$). The jet front is located at $x/\Delta = 1100$.

linear stage of the instability. Figure 2 shows the merging of current components (the front of the nonlinear region) behind the current filaments, where some jet electrons are slightly accelerated, as we shall show in Fig. 4 below. More complicated structures are seen near the jet boundary, that we shall investigate in more detail below.

The three-dimensional morphology of the jet's magnetic field is shown in Figure 3 where we plot magnetic-field vectors at $t = 900 \omega_{pe}^{-1}$ (Fig. 3a) and $t = 1000 \omega_{pe}^{-1}$ (Figs. 3a and 3b). The regions displayed ($820 < x/\Delta < 1120$; $231 < y/\Delta, z/\Delta < 531$) are indicated by the red dashed rectangle in Figure 1b. The plot is clipped at the center of the jet at $y/\Delta = 381$. One can see that the edge of the helical magnetic field in the jet moves from $x/\Delta = 780$ at $t = 900 \omega_{pe}^{-1}$ to $x/\Delta = 830$ at $t = 1000 \omega_{pe}^{-1}$, which is much slower than the jet speed (if moving with the jet velocity, the front at $t = 1000 \omega_{pe}^{-1}$ should be located at $x/\Delta \approx 880$). This seems to indicate that the front edge of the helical magnetic field is peeled off as the jet propagates. This may indicate that the helical magnetic field is braided by kinetic instabilities and subsequently becomes untangled as discussed in Blandford et al. (2017). The untangling of helical magnetic field results from magnetic-reconnection-like phenomena, that push the helical magnetic field away from the center of the jet at the forward position. Two smaller magnetic islands can be identified in the jet shown in Figure 3 (half of the jet is shown). The supplemental movie¹ shows how the helical magnetic field is untangled and magnetic islands evolve along the jet

¹ dBtotByz11MF_011.mp4: the total magnetic fields in the y - z plane; $280 < y/\Delta < 480$, $280 < z/\Delta < 480$

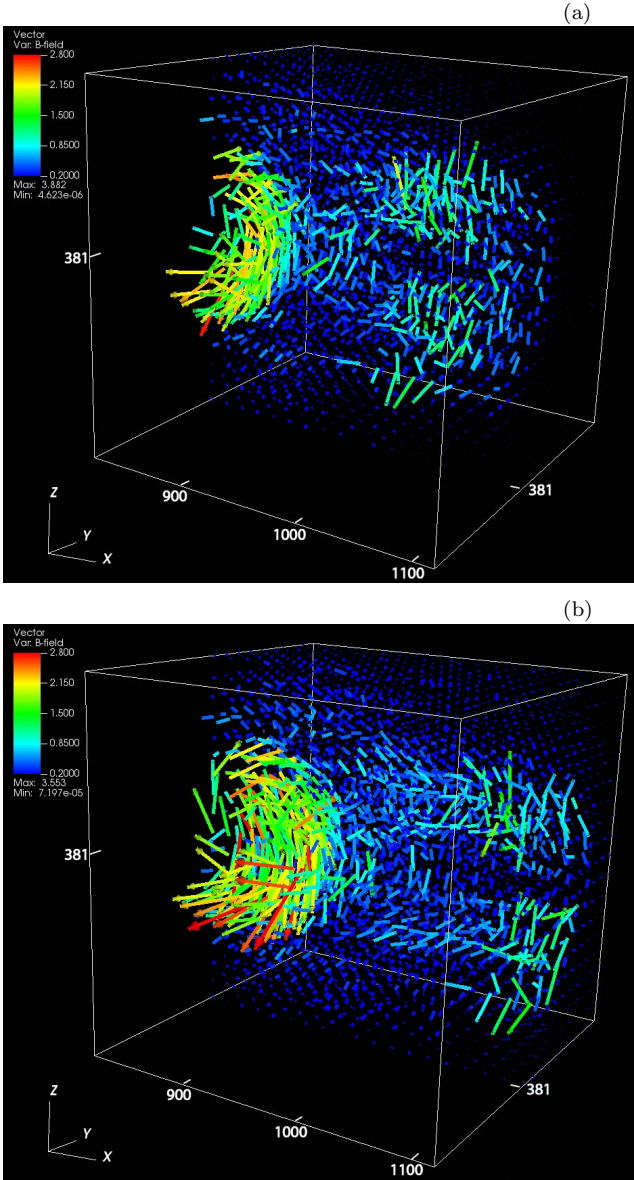


Figure 3. Magnetic-field vectors within a cubic section of the simulation grid ($820 < x/\Delta < 1120$; $231 < y/\Delta, z/\Delta < 531$) at time $t = 900 \omega_{pe}^{-1}$ (a) and at $t = 1000 \omega_{pe}^{-1}$ (b). To illustrate the magnetic field inside the jet, the plots show the rear half of the jet with cut in the $x-z$ plane ($381 < y/\Delta < 531$).

at $t = 1000 \omega_{pe}^{-1}$. For example at $x/\Delta = 950$ the centers of magnetic islands are located around $(y/\Delta, z/\Delta) = (435, 420)$ (upper), $(440, 318)$ (lower) (visible in Fig. 3b), $(320, 350)$, and $(280, 400)$ (not visible).

Figure 4 shows the phase-space distribution of jet (red) and ambient (blue) electrons at $t = 900 \omega_{pe}^{-1}$ and at $t = 1000 \omega_{pe}^{-1}$. Both groups of electrons are accelerated at several locations that coincide with jet recollimation regions (compare Fig. 1a-b). In particular, electrons are accelerated at $x/\Delta = 780$, where the helical magnetic field disappears, as shown in Figure 3a. The disappearance of helical magnetic field near $x = 830\Delta$ also coincides with the acceleration of electrons. Ambient electrons entrained in the relativistic jet plasma are also strongly accelerated.

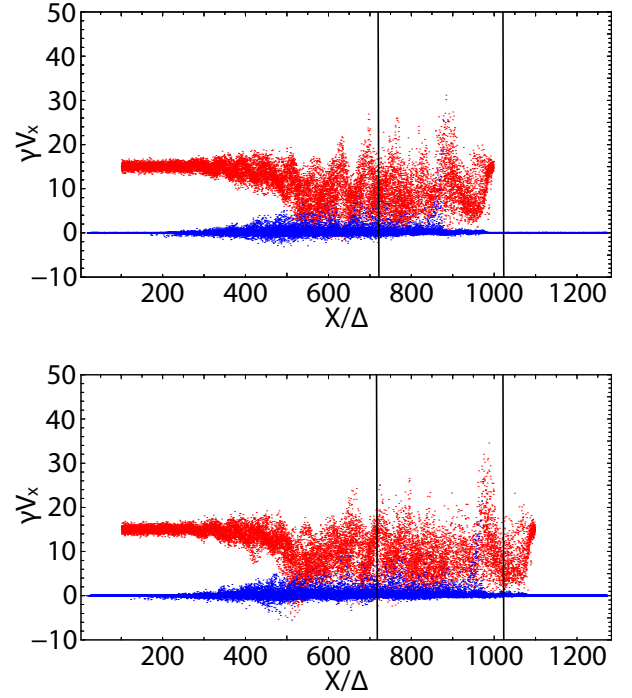


Figure 4. Phase-space ($x - \gamma V_x$) distribution of jet (red) and ambient (blue) electrons at $t = 900 \omega_{pe}^{-1}$ (top) and $t = 1000 \omega_{pe}^{-1}$ (bottom). The two vertical lines show the regions for which Fig. 3 displays the 3D magnetic-field vectors.

To examine how electrons are accelerated in the jet, we plot in Fig. 5 their velocity distribution in the linear and the nonlinear stage. The jet electrons initially have a Lorentz factor $\gamma \approx 15$. The distribution (in red) quickly widens, and some jet electrons are accelerated up to $\gamma = 40$. Surprisingly, the ambient electrons can also be accelerated up to $\gamma = 30$.

Figure 4 suggests that the groups of accelerated jet electrons visible at $t = 900 \omega_{pe}^{-1}$ moved upward to larger x at $t = 1000 \omega_{pe}^{-1}$. These electrons were accelerated at an earlier time. To investigate the process of their acceleration, in Figure 6 we show the correlation between electron acceleration and structures of the electromagnetic field excited by instabilities at $t = 500 \omega_{pe}^{-1}$.

The MI is the dominant instability in the azimuthal direction. Figure 6 shows that it pinches the jet and generates recollimation shocks. Certainly, kKHI is also excited, perturbs the jet, and aids in the creation of three recollimation shocks. Figure 6 features three regions with strong magnetic-field component B_y , at which we can observe also a positive electric-field component E_x . These structures are similar to recollimation shocks in RMHD simulations (Mizuno et al. 2014). The arrows (B_x, B_z) in Figure 6 indicate magnetic-field reversal at $(x/\Delta, z/\Delta) = (440, 390)$. Reconnection in a 3D system is not easily identified in a 2D display, but the evidence in this figure and other diagnostics let's us believe that reconnection takes place. The sequence of evolution is the following: kKHI and MI (WI) grow, and recollimation shocks are generated. At the same time reconnection occurs. The negative quasi-static electric field E_x generated by the recollimation shocks accelerates jet electrons. Electrons are also decelerated where a strong positive E_x exists. We note that

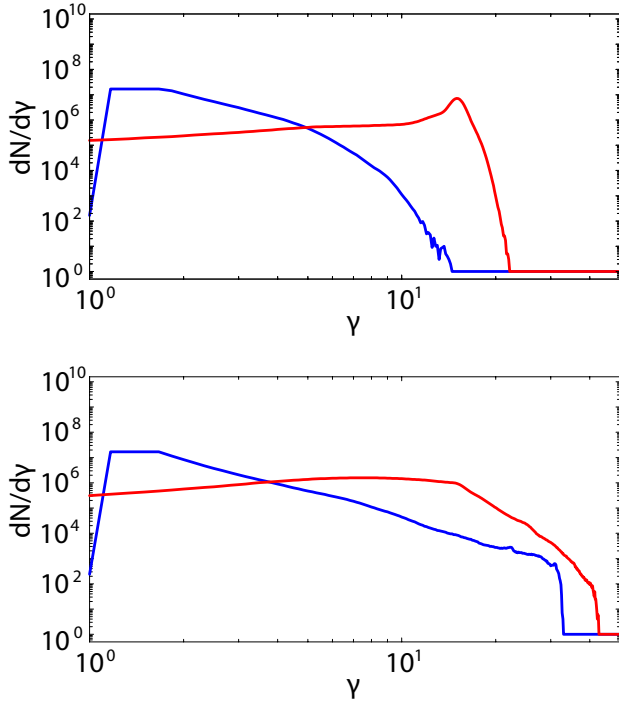


Figure 5. Energy distributions of electrons in the region $x/\Delta < 600$ (top panel) and $x/\Delta > 600$ (bottom panel), corresponding to Fig. 4 at $t = 1000 \omega_{pe}^{-1}$. The red and blue lines show the jet electron and ambient electron velocity distributions, respectively.

the recollimation shocks are not as strong as shocks generated by the WI in slab geometry (compare, e.g., [Ardaneh et al. 2016](#)).

Note that electrons can be further accelerated to higher Lorentz factors on account of turbulent acceleration, as in kinetic simulations of driven magnetized turbulence (e.g., [Comisso & Sironi 2018](#); [Zhdankin et al. 2018](#)). In these simulations turbulent magnetic fluctuations are externally forced in the simulation system, and so the energy source for turbulence is not self-consistent. In contrast to the driven turbulence, in our simulations turbulent magnetic field (multiple magnetic-field islands) are self-consistently generated in the relativistic jet through the untangling of the helical magnetic field. Particles can be directly accelerated in the reconnection regions and also through interactions with the magnetic islands that are visible in, e.g., Figure 1. The particle acceleration processes in turbulent magnetic reconnection have also been investigated by, e.g., [Kowal et al. \(2011, 2012\)](#); [Lazarian et al. \(2016\)](#).

4 SUMMARY

We performed large-scale three-dimensional PIC simulations of an electron-proton jet containing helical magnetic fields. The aim is to investigate in a systematic way how the helical magnetic field in jets evolves and accelerates electrons. The electron-proton jet undergoes kinetic instabilities, the most dominant of which is the MI. It pinches the jet and generates recollimation shocks. The kKHI also operates and contributes to the creation of recollimation shocks. We observed a number of instances of strong transverse magnetic

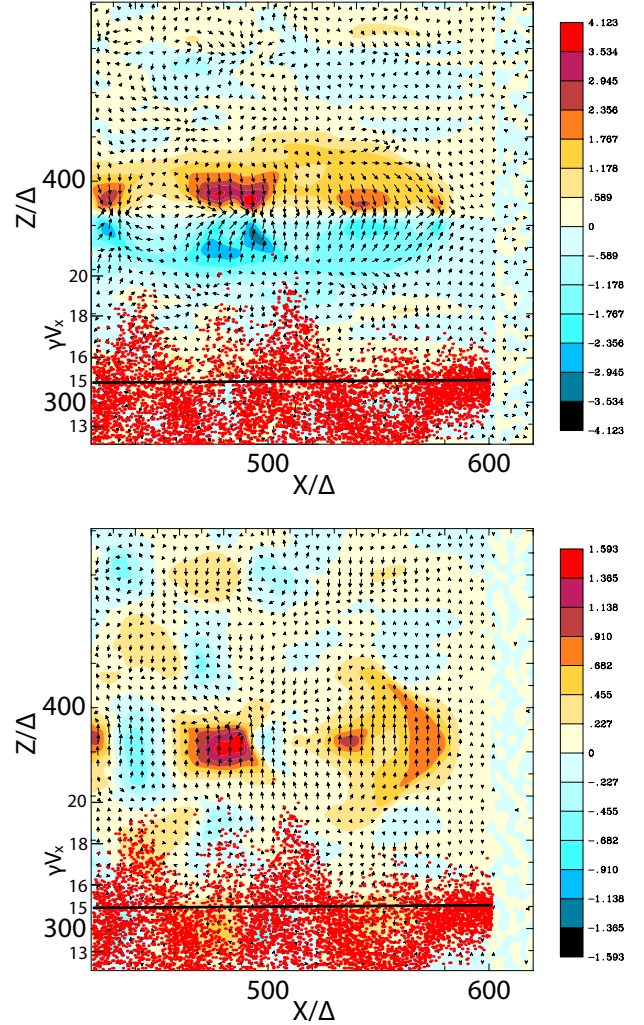


Figure 6. Top panel: Contours of B_y with arrows of $E_{x,z}$. Bottom: E_x with arrows indicating $B_{x,z}$. The $x - \gamma V_x$ distribution of jet electrons at $t = 500 \omega_{pe}^{-1}$ (a) is overplotted in red. Some jet electrons are accelerated up to $v_x \gamma = 20$ above the initial $v_x \gamma = 15$ (the black line) in the phase space. The scale for the phase-space is indicated with small digits at the left axis.

field, B_y , coinciding with significant jet-parallel electric field, E_x , that are similar to the structure of recollimation shocks in RMHD simulations ([Mizuno et al. 2014](#)). Using as tracer magnetic-field reversals and other diagnostics, we found regions in which magnetic reconnection takes place.

It appears that first kKHI and MI (WI) grow, then recollimation shocks are generated, and reconnection operates. The recollimation shocks feature a quasi-static electric field, E_x , that depending on its sign accelerates or decelerates jet electrons. In the nonlinear stage the toroidal magnetic fields are untangled. The disappearance of helical magnetic fields generates magnetic field islands that interact with each other and accelerate electrons. [Kowal et al. \(2011, 2012\)](#); [Lazarian et al. \(2016\)](#) investigated the particle acceleration process in turbulent reconnection theoretically and by numerical experiments. They demonstrated an exponential growth in the energy of the accelerated particles and also the development of a power-law tail in the particle spectrum, both of which

are signatures of stochastic Fermi acceleration by reconnection. Figure 5 shows a power-law tail and hence is consistent with this scenario, but further investigation are needed to confirm stochastic Fermi acceleration.

Recently, de Gouveia Dal Pino et al. (2018); Kadowaki et al. (2018, 2019); Singh et al. (2016) used relativistic MHD simulations with test particles to investigate acceleration through turbulent magnetic reconnection driven by KI. Using PIC simulations Alves et al. (2018, 2019) found that the formation of highly tangled magnetic fields and a large-scale inductive electric field in kink-unstable jets accelerates particles through curvature drift. There is no bulk flow in their simulations, and therefore velocity-shear instabilities such as kKHI and MI are not excited, and KI occurs instead. Since the magnetization in their simulations is very large, $\sigma > 1$, the toroidal magnetic field is dominant and the KI is triggered, which tangles the helical magnetic field and consequently may result in reconnection, and not necessarily only curvature drift acceleration. We should add that the jet density profile assumed in Alves et al. (2018), $n = n_0 + (n_c - n_0)/\cosh^2(2r/R_c)$, differs from the top hat profile that we employ. Our choice may be more conducive to the kKHI, MI, and the Weibel modes.

Since kinetic KHI and MI grow faster than current-driven kink instabilities due to strong velocity shear and moderate magnetization, our simulation does not show a kink-like instability as seen in the simulations of Alves et al. (2018). In our simulation the particles are accelerated by the turbulent magnetic reconnection which is initiated by the growth of kinetic instabilities such as kKHI and MI.

We investigated in a self-consistent fashion one of the possible mechanisms of electron acceleration in relativistic jets containing helical magnetic field. We demonstrated that as the electron-proton jet evolves, the helical magnetic field becomes untangled and locally reconnects. Electrons are accelerated within the resulting turbulent magnetic field. More simulations with larger jet radii are required, in which we vary the magnetic-field structures, for example the characteristic scale, a , and the pitch profile parameter, α . Moreover, a variation of the density profile and the magnetization of the jet are required and will be the subject of future studies.

ACKNOWLEDGEMENTS

We appreciate Christoph Köhn's critical reading and fruitful suggestions which improved the contents of this report. This work is supported by the NASA-NNX12AH06G, NNX13AP-21G, and NNX13AP14G grants. The recent work is also provided by the NASA through Chandra Award Number GO7-18118X (PI: Ming Sun at UAH) issued by the Chandra X-ray Center, which is operated by the SAO for and on behalf of the NASA under contract NAS8-03060. The work of J.N. and O.K. has been supported by Narodowe Centrum Nauki through research project DEC-2013/10/E/ST9/00662. Y.M. is supported by the ERC Synergy Grant "BlackHoleCam: Imaging the Event Horizon of Black Holes" (Grant No. 610058). The work of I.D. has been supported by the NUCLEU project. Simulations were performed using Pleiades and Endeavor facilities at NASA Advanced Supercomputing (NAS: s2004), and using Comet at The San Diego Super-

computer Center (SDSC), and Bridges at The Pittsburgh Supercomputing Center, which are supported by the NSF.

REFERENCES

- Alves, E.P., Grismayer, T., Fonseca, R.A., Silva, L.O. 2015, Phys. Rev. E, 92, 021101
- Alves, E.P., Zrake, J., Fiuza, F., 2018, PRL 121, 245101
- Alves, E.P., Zrake, J., Fiuza, F., 2019, Phys. Plasmas 26, 072105
- Ardaneh, K., Cai, D., Nishikawa, K.I. 2016, ApJ, 827, 124
- Barniol Duran, R., Tchekhovskoy, A., & Giannios, D. 2017, MNRAS 469, 4957
- Birkinshaw, M. 1984, MNRAS, 208, 887
- Birkinshaw, M. 1996, Astrophys Space Sci, 242: 17
- Blandford, R., Yuan, Y., Hoshino, M., Sironi, L. 2017, Space Sci Rev, 207, 291
- Broderick A. E. & Loeb A. 2009, ApJ, 697, 1164
- Buneman, O. 1993, in *Computer Space Plasma Physics: Simulation Techniques and Software*, Eds.: Matsumoto & Omura, Tokyo: Terra, p.67
- Christie, I. M., Lalakos, A., Tchekhovskoy, A., Fernández, R., Foucart, F., Quataert, E., Kasen, D. 2019, MNRAS, 490, 4811
- Comisso, L., Sironi, L., 2018, prl, 121, 255101
- Daughton, W., Roytershteyn, V., Karimabadi, H., et al. 2011, Physics Nature, 7, 539
- de Gouveia Dal Pino, E. M., & Lazarian, A. 2005, A&A 441, 845
- de Gouveia Dal Pino, E. M., Piovezan, P. P., Kadowaki, L. H. S. 2010, A&A, 518, 5
- de Gouveia Dal Pino, E. M., Alves Batista, R., Kowal, G., Medina-Torrejón, T., Ramirez-Rodriguez, J. C. 2018, <https://pos.sissa.it/cgi-bin/reader/conf.cgi?confid=329>
- Drenkhahn, G., & Spruit, H. C. 2002, A&A 391, 1141
- Fowler, T. K., Li, H., Anantua, R. 2019, ApJ, 885, 4
- Fujimoto, K. 2011, J. Compt. Phys., 230, 8508
- Gabuzda, D., 2019, Galaxies, 7, 5
- Giannios, D., Uzdensky, D. A., & Begelman, M. C., MNRAS, 395, L29
- Giannios, D. 2010, MNRAS, 408, L46
- Giannios, D. 2011, J. Phys: Conf. Ser. 283, 012015
- Granot, J., Komissarov, S. S., & Spitkovsky, A. 2011, MNRAS, 411, 1323
- Granot, J. 2012, MNRAS, 421, 2442
- Guo, F., Liu, Y.-H., Daughton, W., & Li, H., 2015, ApJ, 806, 167
- Guo, F., Li, H., Daughton, W., et al., 2016a, ApJL, 818, L9
- Guo, F., Li, H., Daughton, W., Li, X., & Liu, Y.-H., 2016b, PhPl, 23, 5708
- Hawley, J. F., Fendt, C., Hardcastle, M., et al. 2015, Space Sci. Rev., 191, 441
- Kadowaki, L. H. S.; De Gouveia Dal Pino, E. M., Stone, J. M. 2018, ApJ, 864, 52
- Kadowaki, L. H. S., de Gouveia Dal Pino, E. M., Medina-Torrejón, T. E. 2019, <https://pos.sissa.it/cgi-bin/reader/conf.cgi?confid=329>
- Kagan, D., Milosavljevic, M., & Spitkovsky, A. 2013, ApJ, 774, 41
- Karimabadi, H., Roytershteyn, V., Vu, H. X., et al. 2014, PhPl, 21, 2308
- Komissarov, S. S. 2012, MNRAS, 422, 326
- Kowal, G., de Gouveia Dal Pino, E.M., Lazarian, A. 2011, ApJ, 735, 102
- Kowal, G., de Gouveia Dal Pino, E. M., Lazarian, A., 2012, Phys. Rev. Lett., 108, 241102
- Lazarian A., Kowal G., Takamoto M., de Gouveia Dal Pino E.M., Cho J. 2016, Theory and Applications of Non-relativistic and Relativistic Turbulent Reconnection. In: Gonzalez W., Parker E. (eds) Magnetic Reconnection. Astrophysics and Space Science Library, vol 427. Springer, Cham

- Markidis, S., Lapenta, G. Delzanno, G. L., et al. 2014, PPCF, 56, 064010
- McKinney, J. C., & Uzdensky, D. A. 2012, MNRAS, 419, 573
- Mizuno, Y., Hardee, P. E., & Nishikawa, K.-I. 2014, ApJ, 784, 167
- Mościbrodzka, M., Dexter, J., Davelaar, J., & Falcke, H., MNRAS, 468, 221
- Niemiec, J., Pohl, M., Stroman, T., & Nishikawa, K.-I. 2008, ApJ, 684, 1174-1189
- Nishikawa, K.-I., Frederiksen, J. T., Nordlund, Å., et al. 2016a, ApJ, 820, 94
- Nishikawa, K.-I., Mizuno, Y., Niemiec, J., et al. 2016b, Galaxies, 4, 38
- Nishikawa, K.-I., Mizuno, Y., Gómez, J. L., et al. 2017, Galaxies, 5, 58
- Nishikawa, K.-I., Mizuno, Y., Gómez, J. L., et al. 2019, Galaxies, 7, 29
- Oka, M., Fujimoto, T. K., Nakamura, M., et al. 2008, PRL, 101, 205004
- Singh, C. B., Mizuno, Y., & de Gouveia Dal Pino, E., 2016, ApJ, 824, 48
- Sironi, L. & Spitkovsky, A. 2011, ApJ, 741, 39
- Sironi, L., Spitkovsky, A., Arons, J. 2013, ApJ, 771, 54.
- Sironi, L. & Spitkovsky, A. 2014, ApJ, 783, L21
- Sironi, L., Petropoulou, M., & Giannios, D. 2015, MNRAS, 450, 183
- Stone, J. M. & Morman, M. L. 1994, ApJ, 433, 746. Stone, James M.; Norman, Michael L.
- Stone, J. M., Hardee, Philip E. 2000, ApJ, 540, 192
- Tchekhovskoy, A. 2015, ASSL, 414, 45
- Uzdensky, D. A. 2011, Space Sci. Rev., 160, 45
- Wendel, D. E., Olson, D. K., Hesse, M., et al. 2013, PhPl, 20, 2105
- Yao, W., Qiao, B., Zhao, Z., Lei, Z., Zhang, H., Zhou, C., Zhu, S., He1, X., 2019, ApJ, 876, 2
- Zenitani, S. & Hoshino, M. 2005, ApJ, 618, L111
- Zenitani, S. & Hoshino, M. 2008, ApJ, 677, 530
- Zenitani, S., Hesse, M., Klimas, A., & Kuznetsova, M. 2011, PRL, 106, 195003
- Zenitani, S., Shinohara, I., Nagai, T., & Wada, T. 2013, PhPl, 20, 092120
- Zhang, B. & Yan, H. 2011, ApJ, 726, 90
- Zhdankin, V., Uzdensky, D. A., Werner, G. R., Begelman, M. C., 2018, ApJL, 867, L18

This paper has been typeset from a \LaTeX file prepared by the author.